South African Journal of Geology, 2002 (in press)

Mylonitization And Decomposition Of Garnet: Evidence For Rapid Deformation And Entrainment Of Mantle Garnet-Harzburgite By Kimberlite Magma, K1 Pipe, Venetia Mine, South Africa

J. M. Barton Jr.*

Department of Geology, Rand Afrikaans University, P.O. Box 524, Auckland Park 2006, South Africa, jmb@na.rau.ac.za

T.V. Gerya

Institute of Experimental Mineralogy, Russian Academy of Sciences, Chernogolovka, Moscow district, 142432, Russia, taras@iem.ac.ru

Institut für Geologie, Mineralogie und Geophysik, Fakultät für Geowissenschaften, Ruhr-Universität Bochum, 44780 Bochum, Germany, **taras.gerya@ruhr-uni-bochum.de**

South African Journal of Geology, In press

* Corresponding author

Abstract

Sheared and unsheared nodules of garnet-harzburgite from the K1 Venetia kimberlite pipe (South Africa) are composed primarily of olivine and orthopyroxene (partially replaced by serpentine, magnetite and chlorite) and abundant porphyroblasts of garnet with kelyphitic rims of orthopyroxene, clinopyroxene and spinel. When mylonitized, orthopyroxene defines a mineral elongation lineation while bent orthopyroxene and sigmoidal garnet with wings of orthopyroxene define consistent senses of motion within individual nodules. The kelyphite surrounding both undeformed and undeformed garnet grains is not deformed and appears to have resulted from the inversion of garnet and olivine to orthopyroxene, clinopyroxene and spinel, corresponding to the isograd separating garnet peridotite from spinel peridotite. Subsequent hydration around nodule rims and along fractures within nodules resulted in the formation of serpentine, magnetite and chlorite from olivine and orthopyroxene. This hydration is believed to have resulted from reaction with the entraining kimberlite magma. The preservation of mylonite rather than its annealing and recrystallisation to coarse-grained rocks at high temperature strain free mantle conditions requires quenching shortly after mylonite formation. This preservation taken with the presence of undeformed kelyphite around garnet grains implies that mylonitization and entrainment of garnet-harzburgite into kimberlite magma and kelyphite formation occurred during very rapid magma ascent.

Introduction

At the present level of exposure (10 level, ~110 m depth), garnet-harzburgite is the most common mantle nodule composition found within the ~530 Ma (Allsopp *et al.*, 1995) K1 kimberlite pipe at the Venetia Mine, South Africa (Figures 1 and 2). Associated primarily with the earliest phase of hypabyssal kimberlite intrusion as deduced from cross cutting relationships (*e.g.* Seggie *et al.*, 1999) (Figure 3), these nodules range in texture from massive and unsheared to mylonitic (Figure 4). Abundant garnet, whether deformed or not, is always rimmed by undeformed kelyphite (Figure 4E), showing that kelyphite formation postdated deformation. In addition, reaction rims between kimberlite magma and the nodules surround only some of the kelyphitic rims, showing the kelyphite formation is not a result of chemical interaction with kimberlite magma. In this paper we document the nature of mylonitization of garnet-harzburgite, the subsequent generation of kelyphitic rims around undeformed and deformed garnet and then hydration from the kimberlite magma. It is argued that these processes are associated with the rapid, forceful passing of kimberlitic magma through actively deforming garnet-harzburgite on the way to the surface, and then decompression of entrained nodules of this composition.

The K1 Kimberlite Pipe

The K1 kimberlite pipe (Figures 2 and 3) is one of 13 bodies, exposed at surface or blind, presently recognized within the Venetia kimberlite cluster (*e.g.* Seggie *et al.*, 1999). It intruded into >2.0 Ga gneisses and schists of the Central Zone of the Limpopo Belt (*e.g.* Pienaar, 1985; S. Pretorius, 1986; 1992; W. Pretorius, 1996) as well as gabbroic sills and lavas and bodies of sodic pegmatite of various ages between 1.6 and 1.8 Ga age (Pretorius, 1996; Barton and Pretorius, 1997; Twiggs *et al.*, 2002). Composed of "monticellite-phlogopite kimberlite of Group I character", it comprises six hypabyssal and diatreme or tuffaceous kimberlite breccia (TKB) phases (Seggie *et al.*, 1999). While mantle and crustal nodules occur within all six of these phases, they are by far most abundant in earliest hypabyssal-facies phase (H-N and H-S; Figure 3).

The distribution of deep mantle nodules within the kimberlite phases of the K1 pipe is heterogeneous. The collection at the Rand Afrikaans University (RAU), which was sampled primarily from seven level downwards, is dominated by garnet-harzburgite (>80% of ~ 300 nodules) with a few examples of harzburgite, pyroxenite, dunite and eclogite. The smaller collection studied by Stieffenhoffer *et al.* (1998; 1999) at the DeBeers Geoscience Centre (Johannesburg, South Africa) was collected from seven level upwards and is dominated by garnet-lherzolite with lesser amounts of garnet-harzburgite, garnet-spinel peridotite and spinel peridotite, the latter two types presumably from a lower P-T environment.

Garnet-Harzburgite Nodules

After examining thin sections of the entire RAU nodule collection, six nodules of garnet-harzburgite were selected for detailed petrographic study (Figure 4) on the basis of their distinct microstructural features and a low degree of hydration (Table 1). Undeformed to moderately deformed garnet-harzburgite nodules are large ellipsoids or fragments thereof, ranging in size up to 40 x 30 x 20 cm (B-00-184, Figure 4D). As the garnet-harzburgite becomes progressively sheared, its nodules become smaller and more flattened, *e.g.* sample B-00-136, 10 x 5 x 3 cm (Figure 4F). The long and short axes of the sheared nodules define the planes containing the mineral elongation lineations.

The nodules of undeformed garnet-harzburgite are coarse-grained, porphyroblastic rocks composed primarily of large (5 to 10 mm) fractured grains of olivine and 1 to 5 mm isometric grains of pyroxenes with 5 to 10 mm euhedral garnet porphyroblasts. The pyroxenes are mostly orthopyroxene although relatively rare grains of euhedral clinopyroxene occur up to 0.3 cm in long axis. Most clinopyroxene is associated with kelyphitic rims around garnet (see below). Fracturing of olivine grains is accompanied by the development of serpentine in the cracks. Fracturing is not accompanied by the significant displacement of olivine segments. Garnet porphyroblasts are always surrounded by radial kelyphitic aggregates (Figure 5a) composed of pyroxenes and spinel. Similar symplectites also fill cracks in the garnet. The degree of replacement of garnet varies from 10 to 100% and does not depend on the location of the garnet porphyroblasts relatively to the xenolith margins.

In comparison to undeformed nodules of the same mineral composition, deformed garnet-harzburgite nodules are commonly characterized by smaller grain size and a distinct orientation of elongated orthopyroxene grains defining the shear fabric (Figure 6). Reduction of grain size is very characteristic for intensely deformed mylonitized rocks, which also contain abundant shear sense indicators such as bending of the pyroxene grains (Figures 6c and d) and rarely by sigmoid garnet (Figure 6a) and orthopyroxene (Figure 6b) porphyroblasts. Olivine grains in sheared xenoliths are intensely fractured and fragmented (Figures 6b and c). In less deformed rocks olivine fragments are elongated and orientated along the fabric. As with the undeformed nodules, garnet grains are surrounded by 0.1 to 1 mm, radial kelyphytic rims (Figure 5b) that can replace up to 100% of the grains independent of location within the nodule. The radial internal texture of kelyphite clearly suggests their post-shear origin. Cracks in olivine are filled by serpentine. In intensely mylonitized samples, serpentine often composes a significant part of the rock matrix surrounding abundant small random fragments of olivine (Figure 6c).

Darker rims, up to 5 cm wide, occur around the edges of the nodules whether deformed or not and reflect increased serpentine and chlorite and decreased olivine and orthopyroxene content. They resulted from reaction with fluids presumably from the kimberlite magma during transport. These rims surround coarsely crystalline garnet with kelyphitic rims and orthopyroxene crystals without apparent reaction.

Reaction textures

Two types of reaction textures are distinguished in all samples studied:
1) Replacement of garnet by orthopyroxene-clinopyroxene-spinel kelyphite (Figure 5) and
2) Subsequent hydration textures (replacement of olivine by serpentine and magnetite and orthopyroxene by chlorite) superimposed on both initial mineral assemblages (Figures 6b and c) and kelyphitic textures (Figure 7).

The internal structures of kelyphitic rims around garnet are characterized by relatively coarse-grained (5 to 30 μm) outer portions with orthopyroxene, clinopyroxene and spinel without preferred mineral orientation, surrounding cryptocrystalline (<3 μm) radial aggregates of the same minerals replacing garnet (Figure 5). Formation of kelyphitic textures appears to be controlled by diffusion of the components on the garnet-olivine boundaries and related to the retrograde reaction garnet plus olivine goes to orthopyroxene, clinopyroxene and spinel, corresponding to the isograd between garnet peridotite and spinel peridotite assemblages. This reaction seems to be near isochemical in a local scale and not related to significant addition of the components from kimberlitic magma. However, in one instance, a Ba rich phase also occurs within the orthopyroxene-clinopyroxene-spinel kelyphite (Figure 5d). Presently, the origin and significance of the Ba is not understood but Ba-bearing phase may be a distinct hint on metasomatism caused by kimberlitic magma.

Hydration reaction textures are very common for all types of nodules. Although in the inner portions of nodules these reactions are mostly developed along the grain boundaries and cracks inside the minerals, the complete replacement of olivine to serpentine and magnetite and orthopyroxene to chlorite occurs in the altered outer (black) zones of the nodules. These reactions are likely to have resulted from the infiltration of a water bearing fluid during the transport of nodules within kimberlitic magma.

Composition of minerals

Microprobe analyses of coexisting minerals from studied samples were carried out using the CAMECA microprobe and the Scanning Electronic Microscope in the Faculty of Science at Rand Afrikaans University as well as the Electronic Microprobe of the Institute of Geology, Mineralogy and Geophysics at Ruhr-University of Bochum. Table 2 contains representative microprobe analyses of minerals from both deformed (B-00-136, B-00-184) and undeformed (VN17, VN19) samples. Major characteristics of chemical compositions of garnets and pyroxenes from studied samples are summarized in Figures 8 and 9. Most of the matrix minerals are characterized by homogeneous chemical compositions (Figures 8a and b; 9a and b) and by the absence of chemical zoning (Figure 8b). However in the moderately deformed sample B-00-184, systematic zoning of Cr contents is observed in garnet (Figure 8d) and pyroxenes (Table 2).

Compositions of minerals within kelyphitic textures are inhomogeneous and strong zoning of Al and Cr contents is common in relatively large (10 to 30 μm) grains of spinel and pyroxenes composing the outer portions of the symplectites (Figure 9d, Table 2). However, the distribution of Ca, Mg and Fe between clinopyroxene and orthopyroxene is very uniform for all grains studied and is less variable then those detected for matrix minerals (compare Figures 9a and c).

Thermobarometry of the nodules

Methodology

Thermobarometry of mantle nodule is recognized as a complex problem (see review by Smith, 1999) that cannot be solved by simple routine methods applicable for example to lower grade metamorphic rocks (*e.g.* Frost and Chacko, 1989; Spear and Florence, 1992; Spear, 1993). Several authors (*e.g.*, Harley, 1984; Frost and Chacko, 1989; Spear and Florence, 1992; Spear, 1993) have also noted that geothermometers based on Fe-Mg exchange reactions are not likely to quench at the same P-T conditions as geobarometers that are based on net-transfer reactions. Therefore, in these cases, P-T estimates deduced from thermobarometry using mineral compositions affected by late Fe-Mg exchange may give misleading results (*e.g.*, Frost and Chacko, 1989; Spear and Florence, 1992; Spear, 1993). As found by Smith (1999), the accuracy of thermobarometric calculations for garnet peridotite xenoliths is best established for the two pyroxene thermometer plus Al-in-orthopyroxene barometer of Brey and Kohler (1990) and for P-T conditions in the range 20 to 50 kbar and 800 to 1100^{o}C. Therefore, in contrast to previous workers (Stiefenhofer *et al.*, 1999), we used the formulations of Brey and Kohler (1990) to make our basic thermobarometric estimates (Figure 10). However taking into account that the previously estimated ranges of pressure (up to ~70 kbar) and temperature (up to ~1400^{o}C) for mantle nodules from the Venetia kimberlitic pipes (Stiefenhofer *et al.*, 1998) is partially outside of best established P-T region (Smith 1999), we also used alternative P-T estimates summarized in Table 3. For our thermobarometric calculations, we used the PTEXL program (a MS Excel® file program created by T. Koehler and A. Girnis). This program allows to proceeds with geothermobaromety of mantle rocks on the basis of compositions of coexisting minerals given in weight percent. Correction for Fe^{3+} was taken into account as a part of computing procedure.

Results

The results of thermobarometry for four deformed and undeformed nodules are shown in Figure 10. As may be seen, most of nodules are characterized by significant variations in both pressure (42 to 74 kbar) and temperature (1260^o to 1450^{o}C) estimated using the composition of matrix minerals using the same combination of the two-pyroxene thermometer and garnet-orthopyroxene barometer of Brey and Kohler (1990). On the other hand, the maximum P-T estimates are consistent (70 to 74 kbar and 1400^o to 1450^{o}C) and may suggest similar initial conditions of crystallization of garnet-pyroxene assemblage. Variation in P-T estimates in most cases reflects simultaneous decrease in pressure and temperature from estimated peak conditions. This variation may, therefore, be attributed to reflect post-peak decompression/cooling history before the entrapment of the rocks by kimberlitic magma. This decompression and cooling proceeded either under low-strain (undeformed peridotites) or in high-strain (deformed peridotites) conditions. In this respect, formation of deformed peridotites might be genetically related to decompression, representing fragments of deep mantle shear zones controlling (convective?) exhumation of mantle rocks. The significant pressure drops recorded within all deformed nodules supports this possibility (Figures 10c and d). No significant temperature decrease occurred for an ~30 kbar drop in pressure in the deformed sample B-00-194 (Figure 11c). This may be attributed to a partial decoupling of the compositions of coexisting pyroxenes possibly due to kinetic effects (e.g., distinctly higher diffusion rates for the Fe and Mg compared to Ca and Al) hampering re-equilibration of these minerals during the fast exhumation process. On the other hand, a significant 100^o to 150^oC temperature decrease with decreasing pressure is recorded for this same sample using Fe-Mg garnet-orthopyroxene (Harley, 1984), garnet-clinopyroxene (Ellis and Green, 1978; Powell, 1985; Krogh, 1988;) and garnet-olivine (O'Neil and Wood, 1978) Fe-Mg exchange thermometers (Table 3), suggesting a common decompression/cooling evolution for this sample (Figure 10c). Peak pressures of 68 to 74 kbar, estimated for Venetia peridotite samples, are outside of 45 to 60 kbar pressure range ("diamond window", Sobolev *et al.*, 2000) characteristic for garnet-orthopyroxene inclusions in diamond and peridotitic xenoliths containing diamond worldwide. However, taking into account relatively low (± 10 to 15 kbar) accuracy of pressure calculations related to low Al_2O_3 content in analysed orthopyroxenes (Table 2), this discrepancies might be related to the differences in the thermobarometers used.

Temperature estimates for the kelyphitic textures were also determined using the two-pyroxene thermometer of Brey and Kohler (1990). These estimates are consistent for different samples and vary between 1140 to 1260^oC at 15 kbar pressure. Lowest temperatures are recorded for the rims of coexisting minerals (Table 3) that corresponds to the cooling of nodules during the formation of kelyphite at the pressures <17 kbar (see intersection of isolines for two-pyroxene temperature estimates with garnet decomposition curve in Figure 10). Further cooling is recorded by the formation of serpentine whose stability field does not exceed 750^oC in temperature (see Figure 10). For several samples, maximum temperatures recorded by kelyphite are consistent with minimum temperature recorded by matrix minerals (Figure 10b and d), which may suggest a continuous thermal evolution of peridotites before and after entrapment by kimberlitic magma. Together with the absence of annealing of deformation textures, the consistency of temperature estimates may suggest entrapment of nodules during or short after the shearing at a temperature ~1250^oC. If this situation is not a coincidence, it may also suggest a link between deformation of mantle and the formation of the kimberlitic magma.

Conclusion

The P-T evolution inferred from the garnet-harzburgite nodules studied is presented in Figure 11. Two interrelated stages of the evolution are suggested:

1) Pre-entrainment mylonitization followed by
2) Syn-entrainment decompression and subsequent cooling and hydration.

These two stages must have occurred rapidly and were very closely related in time because in the absence of stresses at the temperatures and pressures of mylonite and kelyphite formation, annealing to coarse-grained rocks would occur very rapidly if quenching did not take place (*e.g.* Passchier and Trouw, 1996; Smit and van Reenen, 1997).

It is also seen in Figure 11 that our P-T estimates deviate from the average mantle geotherm suggested by Stiefenhofer *et al.* (1999) for the nodules of Venetia kimberlitic pipes. Taking into account that we used thermometers and barometers that differ from those used by Stiefenhofer *et al.* (1998), the systematic deviation in P-T estimates must be mainly related to the discrepancies of different thermobarometric formulations (see Table 3). On the other hand relatively high temperatures estimated in studied nodules may result from the thermal disturbance of the steady state geotherm (e.g., Franz et al., 1996a, b) by the increased heat flow in the mantle during the kimberlite magmatism. This also coincide with intense contemporaneous deformation of peridotites possibly related to the active mantle convection.

Acknowledgements

De Beers Consolidated Mines and the Venetia Mine provided financial and logistical support for this study. RFBR grant # 00-05-64838 and by an Alexander von Humboldt Foundation Research Fellowship to TVG supported this work. We also acknowledge support by the German Research Society through SFB 526. The authors are grateful to N. V. Sobolev and C. A. Smit for discussion and valuable suggestions. We thank Aggrey Mnyama for greatly assisting JMB in the collection of nodules during several collecting trips. We also appreciate dtailed constructive review by L.Franz.

References

Allsopp, H. L., Smith, C. B., Seggie, A. G., Skinner, E. M. W. and Colgan, E. A. (1995). The emplacement age and geochemical character of the Venetia kimberlite bodies, Limpopo Belt, northern Transvaal, *South African Journal of Geology*, **88**, 238-244.

Barton, J. M., Jr. and Pretorius, W. (1998). Crustal xenoliths in Venetia kimberlite pipes in dicate a décollement at ~ 10 km beneath the Central Zone of the Limpopo Belt, South africa. *South African Journal of Geology*, **101**, 323-327.

Bertrand P. and Mercier J.-C. C. (1985). The mutual solubility of coexisting ortho- and clinopyroxene: toward an absolute geothermometer for the natural system? *Earth and Planetary Science Letters*, **76**, 108-122.

Brey G.P. and Koehler T. (1990). Geothermobarometry in four-phase lherzolites II. New thermobarometers, and practical assessment of existing thermobarometers, *Journal of Petrology*, **31**, 1353-1378.

Ellis D.J. and Green D.H. (1978). An experimental study of the effect of Ca upon garnet-clinopyroxene Fe-Mg exchange equilibria, *Contributions to Mineralogy and Petrology*, **71**, 13-22.

Franz et al. (1996a)

Franz et al. (1996b)

Frost, B.R. and Chacko, T. (1989). The granulite uncertainty principle: limitations on thermobarometry in granulites. *Journal of Geology*, **87**, 435-450.

Harley S.L. (1984). An experimental study of the partitioning of Fe and Mg between carnet and orthopyroxene, *Contributions to Mineralogy and Petrology*, **86**, 358-373.

Koehler T. and Brey G.P. (1990). Calcium exchange between olivine and clinopyroxene calibrated as a geothermobarometer for natural peridotites from 2 to 60 kb with applications, *Geochimica et Cosmochimica Acta*, **54**, 2375-2388.

Krogh E.J. (1988). The garnet-clinopyroxene Fe-Mg-geothermometer – a reinterpretation of existing experimental data, *Contributions to Mineralogy and Petrology*, **88**, 44-48.

MacGregor I. D. (1974). The system $MgO-Al_2O_3-SiO_2$: solubility of Al_2O_3 in enstatite for spinel and garnet peridotite compositions, *American Mineralogist*, **58**, 110-119.

Nickel K. G. and Green, D. H. (1985). Empirical geothermobarometry for garnet peridotites and implications for the nature of the lithosphere, kimberlites and diamonds, *Earth and Planetary Science Letters*, **73**, 158-170.

O'Neill H.St.C. and Wood B.J. (1978). An experimental study of Fe-Mg partitioning between carnet and olivine and its calibration as a geothermometer, *Contributions to Mineralogy and Petrology*, **70**, 58-70.

Passchier, C. W. and Trouw, R. A. J. (1996). *Microtectonics*, Springer-Verlag, Berlin, Germany, 288 pp.

Pienaar, J. C. (1985). *Die geologie van die Alldays omgewing in noord Transvaal.* MSc thesis (unpublished), Rand Afrikaans University, Johannesburg, South Africa, 158 pp.

Powell R. (1985). Regression diagnostics and robust regression in geothermometer/geobarometer calibration: the garnet-clinopyroxene geothermometer revisited, *Journal of Metamorphic Geology*, **3**, 231-243.

Pretorius, S. J. (1986). *Die geologie in the omgewing van Swartwater en die westlike deel van die distrik Messina in the sentrale sone van die Limpopo-goedel.* MSc. Thesis (unpublished), Rand Afrikaans University, Johannesburg, South Africa, 194 pp.

Pretorius, S. J. (1992). Die lithologie, struktuur en metamorphose van die Komplex Beitbrug wes van Messina en oos van Swartwater. *Bulletin*, *Geological Survey of South Africa*, **105**, 40 pp.

Pretorius, W. (1996). A geochemical and geophysical investigation of a suite of crustal and upper mantle nodules from Venetia kimberlite pipes, Limpopo Belt, South Africa.

MSc thesis (unpublished), Rand Afrikaans University, Johannesburg, South Africa, 275 pp.

Rodionov, A. S. and Viljoen, K. S. (1998). Venetia megacrysts, Northern Province, South Africa. *Extended Abstracts, 7th International Kimberlite Conference, Cape Town, South Africa*, 743-745.

Schmidt, M.W. and Poli, S. (1998). Experimentally based water budgets for dehydrating slabs and consequences for arc magma generation. *Earth and Planetary Science Letters*, **163**, 361-378.

Seggie, A. G., Hannweg, G. W., Colgan, E. A. and Smith, C. B. (1999). The geology and geochemistry of the Venetia kimberlite cluster, Northern Province, South Africa. *Proceedings of the VIIth International Kimberlite Conference, Organizing Committee IKC VII*, Cape Town, South Africa, 750-756.

Smit, C. A. and Van Reenen, D. D. (1997). Deep crustal shear zones, high-grade tectonics and associated metasomatic alteration in the Limpopo Belt, South Africa: Implications for deep crustal processes, *Journal of Geology*, **105**, 37-57.

Smith, D. (1999). Temperatures and pressures of mineral equilibration in peridotite xenoliths: review, discussion, and implications. *In:* Y.Fei, C.M.Bertka and B.O.Mysen (Editors), Mantle Petrology: Field Observations and High Pressure Experimentation: A Tribute to Francis R (Joe) Boyd. *The Geochemical Society Special Publication*, **6**, 171-198.

Sobolev, N.V., Fursenko, B.A., Goryainov, S.V., Shu, J.F., Hemley, R.J., Mao, H.K., Boyd, F.R. (2000) Fossilized high pressure from the Earth's deep interior: The coesite-in-diamond barometer. *Proceedings of the National Academy of Sciences of the United States of America*, **87**, 11975-11978.

Spear, F. S. (1993). *Metamorphic phase equilibria and pressure-temperature-time paths*. Mineralogical Society of America Publication, Washington, D.C. 788p.

Spear, F. S. and Florence, F. P. (1992). Thermobarometry in granulites: pitfalls and new approaches. *Precambrian Research*, **55**, 208-241.

Stiefenhoffer, J., Viljoen, K. S., Tainton, K. M., Dobbe, R. and Hanweg, G. N. (1998). The petrology of a mantle xenolith suite from Venetia, South Africa. *Extended Abstracts, 7th International Kimberlite Conference*, Cape Town, South Africa, 868-870.

Stiefenhoffer, J., Viljoen, K. S., Tainton, K. M., Dobbe, R. and Hanweg, G. N. (1999). The petrology of a mantle xenolith suite from Venetia, South Africa. *Proceedings of the VIIth International Kimberlite Conference, Organizing Committee IKC VII*, Cape Town, South Africa 836-845.

Taylor W. R. (1998). An experimental test of some geothermometer and geobarometer formulations for upper mantle peridotites with application to the thermobarometry of fertile lherzolite and garnet websterite, *Neues Jahrbook für Mineralogie Abhandlung*, **172**, 381-408.

Twiggs, C., Doorgapershad, A., Barnett, W., Barton, E. S. and Barton, J. M., Jr. (2002). The nature and tectonic significance of pegmatite in the country rocks of the Venetia kim berlite pipes. *South African Journal of Geology*, **105**, (in press, this volume)

Viljoen, K. S., Phillips, D., Harris, J. W. and Robinson, N. (1998). Mineral inclusions in diamonds from Venetia kimberlites, Northern Province, South Africa. *Proceedings of the VIIth International Kimberlite Conference, Organizing Committee IKC VII*, Cape Town, South Africa 888-885.

Wells, P. R. A. (1977). Pyroxene thermometry in simple and complex systems, *Contributions to Mineralogy and Petrology*, **62**, 128-138.

Table 1. Mineral textures and assemblages of garnet-harzburgite nodules studied.

Sample	Rock type	Mineral assemblage
VN17	Undeformed, coarse-grained	Ol+Opx+Grt (with kelyphite)+Cpx+(Serp+Mag+Chl)
VN19	Undeformed, coarse-grained	Ol+Opx+Grt (with kelyphite)+Cpx+(Serp+Mag+Chl)
B-00-133	Moderately deformed, coarse-grained	Ol+Opx+Grt (with kelyphite)+Cpx+(Serp+Mag+Chl)
B-00-134	Undeformed, coarse-grained	Ol+Opx+Grt (with kelyphite)+Cpx+(Serp+Mag+Chl)
B-00-136	Strongly deformed (mylonitized), medium-grained	Ol+Opx+Grt (with kelyphite)+Cpx+(Serp+Mag+Chl)
B-00-184	Moderately deformed, coarse-grained	Ol+Opx+Grt (with kelyphite)+Cpx+(Serp+Mag+Chl)

Table 2. Selected microprobe analyses of coexisting minerals in samples studied.

Sample	B-00-136							B-00-184												
Location	Matrix				Kelyphite			Matrix								Kelyphite				
Mineral	Ol	Opx	Cpx	Grt	Opx	Cpx	Spl	Ol (core)	Ol (rim)	Opx (core)	Opx (rim)	Cpx (core)	Cpx (rim)	Grt (core)	Grt (rim)	Opx	Cpx (core)	Cpx (rim)	Spl (core)	Spl (rim)
Spot	B33	B37a	B35	B17c	B12a	B13a	B11a	N35	N28	N43	N29	N37	N42	N25	N26	N6	N1	N2	N3	N4
	Weight %*																			
SiO_2	41.23	57.57	54.08	41.24	56.18	50.69	0.19	40.91	41.05	57.06	57.93	56.08	55.28	42.49	42.29	51.36	56.07	50.15	0.29	0.58
TiO_2	0.02	0.01	0.18	0.06	0.05	0.26	0.26	0.18	0.00	0.09	0.00	0.30	0.40	0.29	0.58	0.19	0.00	0.20	0.19	0.19
Al_2O_3	0.05	0.87	1.66	16.45	2.49	6.60	37.43	<0.11	0.00	1.30	1.19	2.21	2.21	21.49	20.03	10.11	2.21	9.02	46.58	46.83
FeO	8.61	5.34	4.08	6.69	5.64	3.89	12.67	9.09	8.77	5.40	4.93	3.53	3.94	6.48	6.73	6.54	3.22	3.56	11.96	11.86
MnO	0.12	0.16	0.18	0.29	0.25	0.23	0.27	0.18	0.09	0.19	0.47	0.40	0.20	0.67	0.29	0.47	0.30	0.20	0.29	0.19
MgO	49.36	34.04	21.31	19.02	31.58	16.71	17.11	49.32	49.64	33.58	33.85	19.94	19.46	21.52	21.49	29.16	19.58	15.51	19.41	19.63
CaO	0.11	1.39	17.01	7.31	2.49	18.63	0.12	0.00	0.07	1.28	1.12	15.59	15.95	4.73	4.44	1.66	17.31	20.18	0.08	0.23
Na_2O	0.03	0.05	0.38	0.00	0.07	0.50	0.02	0.06	0.06	0.12	0.18	0.65	0.65	0.06	0.06	0.12	0.45	0.39	0.00	0.06
K_2O	0.01	0.00	0.13	0.00	0.01	0.02	0.02	0.00	<0.09	<0.09	0.00	0.00	<0.10	0.00	0.00	0.00	0.00	0.00	<0.10	0.00
Cr_2O_3	0.08	0.46	0.92	8.92	1.16	2.47	31.73	<0.16	<0.23	0.88	0.32	1.29	1.80	2.28	4.08	0.40	0.86	0.78	21.11	20.42
NiO	0.38	0.11	0.07	0.02	0.07	0.00	0.19	n.a**.	n.a.	n.a.	n.a.	n.a.	n.a.	n.a.	n.a.	n.a.	n.a.	n.a.	n.a.	n.a.
	Cations***																			
Si	1.006	1.983	1.949	3.012	1.948	1.841	0.005	0.999	1.001	1.969	1.990	1.998	1.981	3.012	3.013	1.786	2.000	1.815	0.008	0.016
Ti	0.000	0.000	0.005	0.004	0.001	0.007	0.005	0.003	0.000	0.002	0.000	0.008	0.011	0.015	0.031	0.005	0.000	0.006	0.004	0.004
Al	0.001	0.035	0.071	1.416	0.102	0.283	1.250	<0.003	0.000	0.053	0.048	0.093	0.093	1.795	1.682	0.414	0.093	0.385	1.488	1.491
Fe****	0.176	0.154	0.123	0.408	0.164	0.118	0.300	0.186	0.179	0.156	0.142	0.105	0.118	0.384	0.401	0.190	0.096	0.108	0.271	0.268
Mn	0.002	0.005	0.006	0.018	0.007	0.007	0.006	0.004	0.002	0.006	0.014	0.012	0.006	0.040	0.017	0.014	0.009	0.006	0.007	0.004
Mg	1.794	1.748	1.145	2.071	1.633	0.905	0.722	1.796	1.805	1.727	1.733	1.059	1.039	2.274	2.282	1.511	1.041	0.837	0.784	0.790
Ca	0.003	0.051	0.657	0.572	0.093	0.725	0.004	0.000	0.002	0.047	0.041	0.595	0.612	0.359	0.339	0.062	0.662	0.783	0.002	0.007
Na	0.001	0.004	0.027	0.000	0.005	0.035	0.001	0.003	0.003	0.008	0.012	0.045	0.045	0.008	0.009	0.008	0.031	0.028	0.000	0.003
K	0.000	0.000	0.006	0.000	0.000	0.001	0.001	0.000	<0.003	<0.004	0.000	0.000	0.005	0.000	0.000	0.000	0.000	0.000	<0.003	0.000
Cr	0.002	0.013	0.026	0.515	0.032	0.071	0.711	<0.003	<0.004	0.024	0.009	0.036	0.051	0.128	0.230	0.011	0.024	0.022	0.452	0.436
Ni	0.007	0.003	0.002	0.001	0.002	0.000	0.004	n.a.	n.a.	n.a.	n.a.	n.a.	n.a.	n.a.	n.a.	n.a.	n.a.	n.a.	n.a.	n.a.
Sum	2.993	3.995	4.014	8.018	3.986	3.993	3.010	2.996	2.999	3.996	3.988	3.952	3.961	8.016	8.004	4.001	3.957	3.989	3.020	3.019

Table 2. (continued)

Sample	VN17									VN19									
Location	Matrix				Kelyphite					Matrix				Kelyphite					
Mineral	Ol	Opx	Cpx	Grt	Opx	Cpx (core)	Cpx (rim)	Spl (core)	Spl (rim)	Ol	Opx	Cpx	Grt	Opx (core)	Opx (rim)	Cpx (core)	Cpx (rim)	Spl (core)	Spl (rim)
Spot	A51	A49	A50	A53	A9	A2	A5	A12	A11	H3	H38	H36	H1	H15	H20	H16	H31	H13	H14
Weight %																			
SiO_2	41.48	57.36	55.45	42.50	53.94	49.85	48.98	0.09	0.09	41.37	57.92	54.18	41.48	49.94	49.91	46.54	46.32	0.10	0.10
TiO_2	0.09	0.00	0.00	0.38	0.38	0.71	1.01	0.37	0.38	0.00	0.19	0.51	0.58	0.38	0.38	1.22	1.32	0.10	0.19
$Al2O_3$	0.00	0.98	1.99	20.15	6.04	8.17	8.61	57.18	52.63	0.00	0.76	1.52	18.97	10.02	9.76	10.77	11.96	46.89	48.22
FeO	8.73	5.20	4.05	7.20	6.30	3.79	4.50	10.16	10.73	7.94	4.73	3.31	6.25	5.80	6.37	4.13	3.40	10.47	10.45
MnO	0.09	0.19	0.00	0.19	0.38	0.30	0.40	0.37	0.19	0.09	0.38	0.10	0.29	0.47	0.29	0.61	0.51	0.19	0.39
MgO	49.31	34.25	19.59	21.37	30.29	16.63	17.49	20.67	19.97	50.39	34.37	19.89	21.04	28.96	28.56	14.58	13.81	19.25	19.20
CaO	0.07	1.43	17.03	4.44	2.13	18.65	17.71	0.00	0.08	0.15	1.05	18.64	5.56	1.66	1.82	18.30	20.61	0.00	0.15
Na_2O	0.06	0.18	0.59	0.06	0.06	0.33	0.26	0.00	0.00	0.06	0.12	0.39	0.06	0.12	0.00	0.07	0.07	0.00	0.00
K_2O	<0.09	0.00	<0.10	<0.10	0.00	<0.10	<0.10	0.00	0.00	0.00	0.00	0.00	0.00	0.00	0.00	0.00	<0.10	0.00	0.00
Cr_2O_3	0.08	0.40	1.21	3.59	0.49	1.46	0.94	11.16	15.93	0.00	0.48	1.46	5.76	2.65	2.91	3.80	1.90	23.01	21.31
NiO	n.a.	n.a.	n.a.	n.a.	n.a.	n.a.	n.a.	n.a.	n.a.	n.a.	n.a.	n.a.	n.a.	n.a.	n.a.	n.a.	n.a.	n.a.	n.a.
Cations																			
Si	1.010	1.976	1.988	3.029	1.873	1.807	1.778	0.002	0.002	1.004	1.988	1.954	2.979	1.746	1.749	1.705	1.694	0.003	0.003
Ti	0.002	0.000	0.000	0.021	0.010	0.019	0.028	0.007	0.007	0.000	0.005	0.014	0.031	0.010	0.010	0.034	0.036	0.002	0.004
Al	0.000	0.040	0.084	1.692	0.247	0.349	0.368	1.743	1.636	0.000	0.031	0.064	1.606	0.413	0.403	0.465	0.515	1.492	1.527
Fe	0.178	0.150	0.121	0.429	0.183	0.115	0.137	0.220	0.237	0.161	0.136	0.100	0.375	0.169	0.187	0.126	0.104	0.236	0.235
Mn	0.002	0.006	0.000	0.012	0.011	0.009	0.012	0.008	0.004	0.002	0.011	0.003	0.018	0.014	0.008	0.019	0.016	0.004	0.009
Mg	1.790	1.758	1.047	2.270	1.568	0.899	0.946	0.797	0.785	1.823	1.759	1.069	2.253	1.510	1.492	0.796	0.753	0.775	0.769
Ca	0.002	0.053	0.654	0.339	0.079	0.724	0.689	0.000	0.002	0.004	0.039	0.720	0.428	0.062	0.068	0.718	0.807	0.000	0.004
Na	0.003	0.012	0.041	0.009	0.004	0.023	0.018	0.000	0.000	0.003	0.008	0.027	0.009	0.008	0.000	0.005	0.005	0.000	0.000
K	<0.003	0.000	<0.005	<0.009	0.000	<0.005	<0.005	0.000	0.000	0.000	0.000	0.000	0.000	0.000	0.000	0.000	<0.005	0.000	0.000
Cr	0.002	0.011	0.034	0.203	0.013	0.042	0.027	0.228	0.332	0.000	0.013	0.042	0.327	0.073	0.081	0.110	0.055	0.491	0.453
Ni	n.a.	n.a.	n.a.	n.a.	n.a.	n.a.	n.a.	n.a.	n.a.	n.a.	n.a.	n.a.	n.a.	n.a.	n.a.	n.a.	n.a.	n.a.	n.a.
Sum	2.990	4.005	3.975	8.012	3.989	3.992	4.008	3.005	3.006	2.997	3.989	3.993	8.027	4.005	3.999	3.977	3.990	3.004	3.004

* all analyses are normalized to 100 wt.%

** n.a. – not analysed

*** formulas are calculated: Ol and Spl – per 4 O; Opx and Cpx – per 6 O; Grt – per 12 O

**** all Fe is calculated as Fe^{2+}, correction for Fe3+ was taken into account for geothermobarometry as a part of standard procedure by using PTEXL program

Table 3. Results of thermobarometry of samples studied.

Sample	Minerals					T (^{o}C) calculated at P given											P (kbar) calculated at T given				T and P calculated	
	Location	Ol	Opx	Cpx	Grt	P kbar	T [BK_T]	T [KB_T]	T [Kr_T]	T [NW_T]	T [Ha_T]	T [EG_T]	T [Po_T]	T [We_T]	T [BM_T]	T [Ta_T]	T ^{o}C	P [BK_P]	P [NG_P]	P [MC_P]	T^{o}C [BK_T]	P kbar [BK_P]
VN17	Matrix	a59	a58	a57	a52	40	1338	1232	1140	1277	1179	1197	1187	1249	1325	1422	1100	47	48	49	1400	67
						80	1429	1470	1333	1414	1455	1365	1353	1249	1386	1422	1500	74	71	75		
VN17	Matrix	A51	A49	A50	A53	40	1355	1234	1296	1175	1079	1320	1319	1268	1321	1435	1100	47	48	48	1428	70
						80	1454	1472	1509	1322	1336	1502	1499	1268	1381	1435	1500	75	70	73		
VN17	Matrix	A54	A55	A50	A53	40	1355	1352	1296	1184	1079	1320	1319	1268	1321	1435	1100	47	48	48	1428	70
						80	1454	1609	1509	1330	1336	1502	1499	1268	1381	1435	1500	75	70	73		
VN17	Matrix	A54	A60	A57	A52	40	1338	1232	1129	1207	1121	1178	1167	1256	1329	1427	1100	48	49	46	1405	70
						80	1429	1470	1317	1350	1385	1342	1329	1256	1391	1427	1500	76	71	71		
VN17	Matrix	A54	A56	A50	A53	40	1355	1352	1296	1184	1071	1320	1319	1264	1318	1434	1100	46	47	46	1423	68
						80	1453	1609	1509	1330	1326	1502	1499	1264	1377	1434	1500	73	69	71		
VN17	Matrix	A59	A60	A57	A22	40	1338	1232	1129	1207	1121	1178	1167	1256	1329	1427	1100	48	49	46	1405	70
						80	1429	1470	1317	1350	1385	1342	1329	1256	1391	1427	1500	76	71	71		
VN17	Kelyphite		A9	A2		10	1212							1185	1211	1435						
						30	1260							1185	1239	1435						
VN17	Kelyphite		A10	A2		10	1198							1216	1204	1483						
						30	1246							1216	1231	1483						
VN17	Kelyphite		A9	A5		10	1245							1219	1250	1452						
						30	1296							1219	1278	1452						
VN17	Kelyphite		A10	A5		10	1231							1251	1242	1496						
						30	1282							1251	1270	1496						
VN19	Matrix	H3	H38	H36	H1	40	1302	1334	1296	1232	1117	1295	1293	1215	1262	1381	1100	55	56	51	1379	74
						80	1392	1587	1498	1370	1379	1470	1466	1215	1319	1381	1500	82	78	77		
VN19	Matrix	H39	H38	H37	H2	40	1317	1220	1337	1407	1179	1332	1332	1233	1282	1391	1100	54	56	51	1393	74
						80	1408	1456	1547	1525	1453	1512	1510	1233	1341	1391	1500	81	78	77		
VN19	Matrix	H21	H42	H41	H26	40	1310	1334	1242	966	1219	1252	1247	1236	1293	1402	1100	42	45	48	1346	56
						80	1398	1588	1438	1123	1501	1423	1415	1236	1353	1402	1500	65	64	73		
VN19	Matrix	H25	H42	H40	H1	40	1273	1211	1125	936	1196	1157	1145	1200	1259	1375	1100	43	45	48	1303	55
						80	1356	1446	1305	1094	1473	1316	1302	1200	1318	1376	1500	66	64	73		
VN19	Matrix	H21	H22	H40	H1	40	1288	1327	1125	942	1022	1157	1145	1203	1257	1376	1100	41	44	46	1316	53
						80	1372	1579	1305	1100	1266	1316	1302	1203	1316	1376	1500	64	62	71		
VN19	Matrix	H25	H24	H41	H2	40	1334	1218	1269	1004	1001	1278	1274	1237	1291	1400	1100	50	52	51	1397	68
						80	1423	1453	1470	1160	1241	1452	1446	1237	1350	1400	1500	75	73	77		
VN19	Kelyphite		H15	H16		10	1230							1193	1208	1494						
						30	1283							1193	1234	1494						
VN19	Kelyphite		H12	H16		10	1225							1191	1208	1492						
						30	1278							1191	1234	1492						
VN19	Kelyphite		H20	H31		5	1113							1089	1080	1395						
						25	1160							1089	1103	1395						

Table 3. (continued)

Sample	Minerals					T (°C) calculated at P given											P (kbar) calculated at T given				T and P calculated	
	Location	Ol	Opx	Cpx	Grt	P kbar	T [BK$_T$]	T [KB$_T$]	T [Kr$_T$]	T [NW$_T$]	T [Ha$_T$]	T [EG$_T$]	T [Po$_T$]	T [We$_T$]	T [BM$_T$]	T [Ta$_T$]	T °C	P [BK$_P$]	P [NG$_P$]	P [MC$_P$]	T°C [BK$_T$]	P kbar [BK$_P$]
B-00-136	Matrix	B33	B32	B31	B18a	40	1234	1280	1365	1211	1119	1320	1321	1119	1175	1324	1100	45	49	51	1263	53
						80	1322	1525	1562	1346	1377	1491	1489	1119	1225	1324	1500	65	65	78		
B-00-136	Matrix	B33	B37	B36	B17c	40	1283	1285	1290	1196	1099	1262	1259	1197	1249	1379	1100	47	51	51	1324	58
						80	1372	1531	1479	1333	1355	1427	1421	1197	1305	1379	1500	68	67	77		
B-00-136	Matrix	B33	B26	B25	B17b	40	1351	1303	1318	1225	1121	1282	1280	1284	1340	1443	1100	52	56	49	1421	70
						80	1444	1552	1509	1359	1381	1449	1444	1284	1402	1443	1500	74	74	75		
B-00-136	Matrix	B33	B37a	B35	B17c	40	1354	1305	1385	1196	1106	1337	1338	1279	1332	1434	1100	44	47	49	1397	58
						80	1450	1555	1585	1333	1363	1509	1509	1279	1393	1434	1500	63	63	75		
B-00-136	Matrix	B33	B32	B31s	B18a	40	1268	1280	1405	1211	1119	1352	1354	1157	1213	1366	1100	45	49	51	1303	55
						80	1359	1526	1607	1346	1377	1526	1527	1157	1266	1366	1500	65	65	78		
B-00-136	Kelyphite		B20	B23		10	1222							1142	1193	1418						
						30	1274							1142	1218	1419						
B-00-136	Kelyphite		B12a	B13a		10	1220							1160	1201	1404						
						30	1269							1160	1227	1404						
B-00-136	Kelyphite		B14	B10a		10	1188							1126	1159	1375						
						30	1238							1126	1184	1375						
B-00-184	Matrix	N35	N43	N37	N25	40	1379	204	1279	1422	1230	1300	1298	1318	1378	1462	1100	47	47	44	1451	70
						80	1475	313	1487	1539	1515	1479	1475	1318	1442	1462	1500	73	69	67		
B-00-184	Matrix	N28	N34	N38	N26	40	1386	1251	1144	1276	1148	1195	1186	1329	1391	1468	1100	39	41	45	1429	59
						80	1479	1492	1335	1412	1418	1363	1351	1329	1457	1468	1500	63	61	69		
B-00-184	Matrix	N36	N33	N39	N12	40	1387	205	1275	1316	1176	1291	1289	1340	1384	1472	1100	29	30	45	1395	43
						80	1483	313	1481	1446	1450	1468	1463	1340	1449	1472	1500	48	47	69		
B-00-184	Matrix	N28	N29	N42	N26	40	1381	1243	1341	1276	1109	1356	1357	1295	1352	1442	1100	27	30	45	1385	42
						80	1480	1482	1560	1412	1371	1541	1542	1295	1415	1442	1500	47	47	69		
B-00-184	Kelyphite		N21	N24		10	1216							1276	1247	1548						
						30	1265							1276	1275	1548						
B-00-184	Kelyphite		N22	N24		10	1227							1240	1240	1509						
						30	1276							1240	1269	1509						
B-00-184	Kelyphite		N6	N2		5	1119							1127	1097	1426						
						25	1165							1127	1120	1426						
B-00-184	Kelyphite		N7	N1		10	1235							1377	1296	1539						
						30	1280							1377	1327	1539						

Geothermometers used: [BK$_T$] – Opx-Cpx (Brey and Köhler, 1990); [Kr$_T$] – Cpx-Grt (Krogh, 1988); [NW$_T$] – Ol-Grt (O'Neil and Wood, 1979); [KB$_T$] – Ol-Cpx (Köhler and Brey, 1990); [Ha$_T$] – Opx-Grt (Harley, 1984); [EG$_T$] – Cpx-Grt (Ellis and Green, 1979); [Po$_T$] – Cpx-Grt (Powell, 1985); [We$_T$] – Opx-Cpx (Wells, 1977); [BM$_T$] – Opx-Cpx (Bertrand and Mercier, 1985); [Ta$_T$] – Opx-Cpx (Taylor, 1998).

Geobarometers used: [BK$_P$] – Opx-Grt (Brey and Köhler, 1990); [NG$_P$] – Opx-Grt (Nickel and Green, 1985); [Mc$_p$] – Opx-Grt (McGregor, 1974).

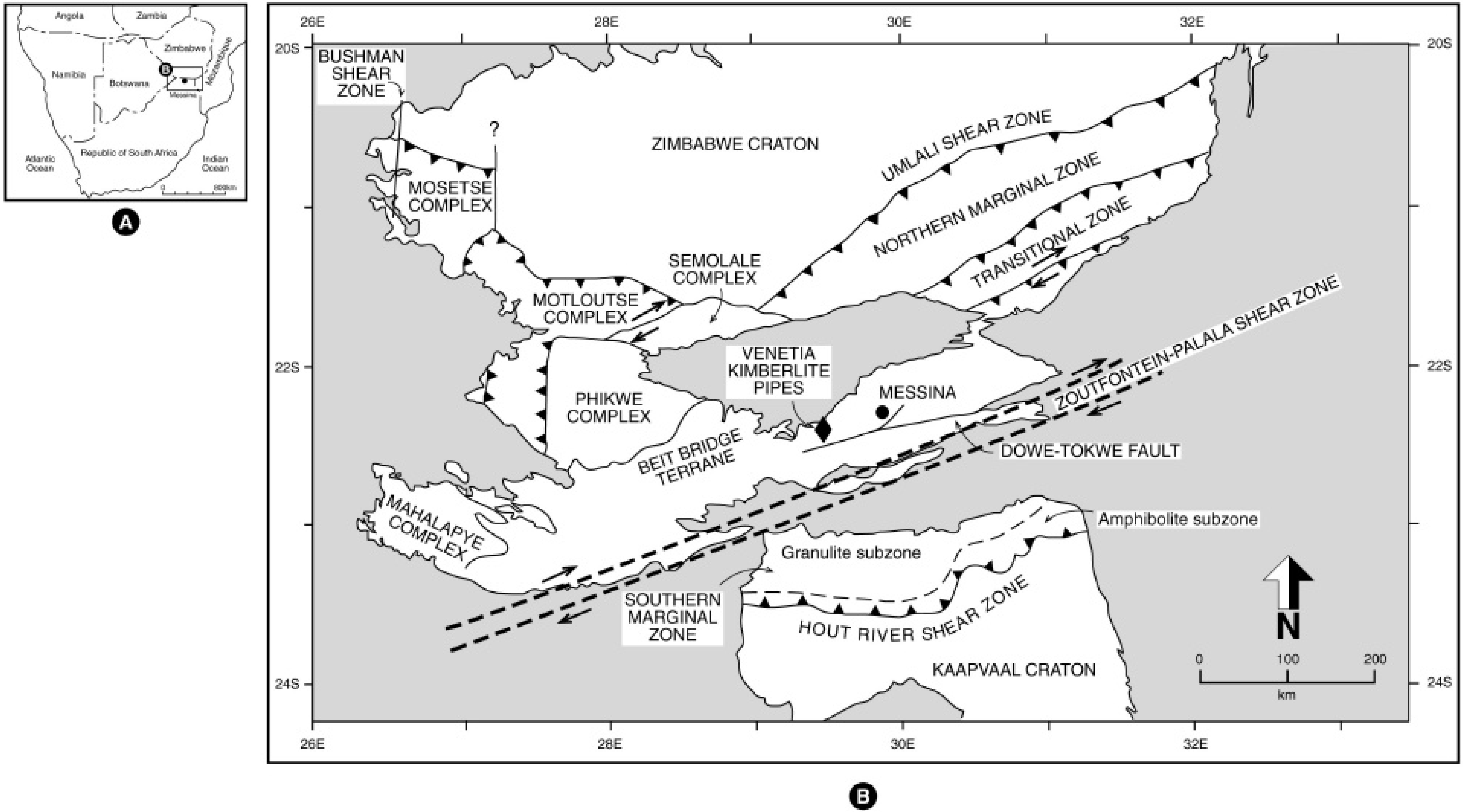

Figure 1: Map showing the location of the Venetia kimberlite cluster within the tectonic units of southern Africa (modified from Barton and Pretorius, 1998).

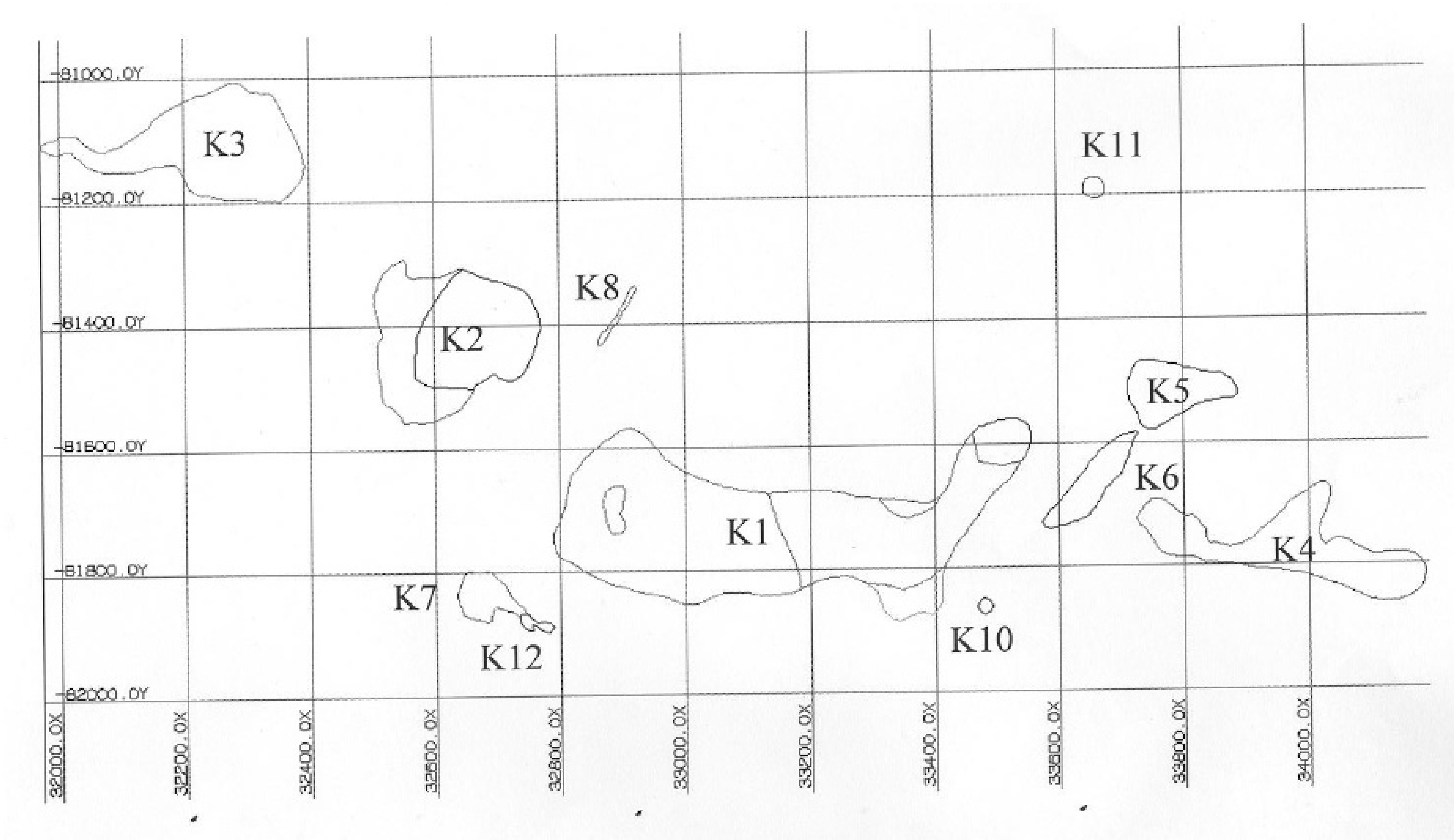

Figure 2: Map showing the location of eleven of the thirteen kimberlite bodies comprising the Venetia cluster within the regional geology. The bodies are oriented using the local north-south grid and each square is 200 m^2.

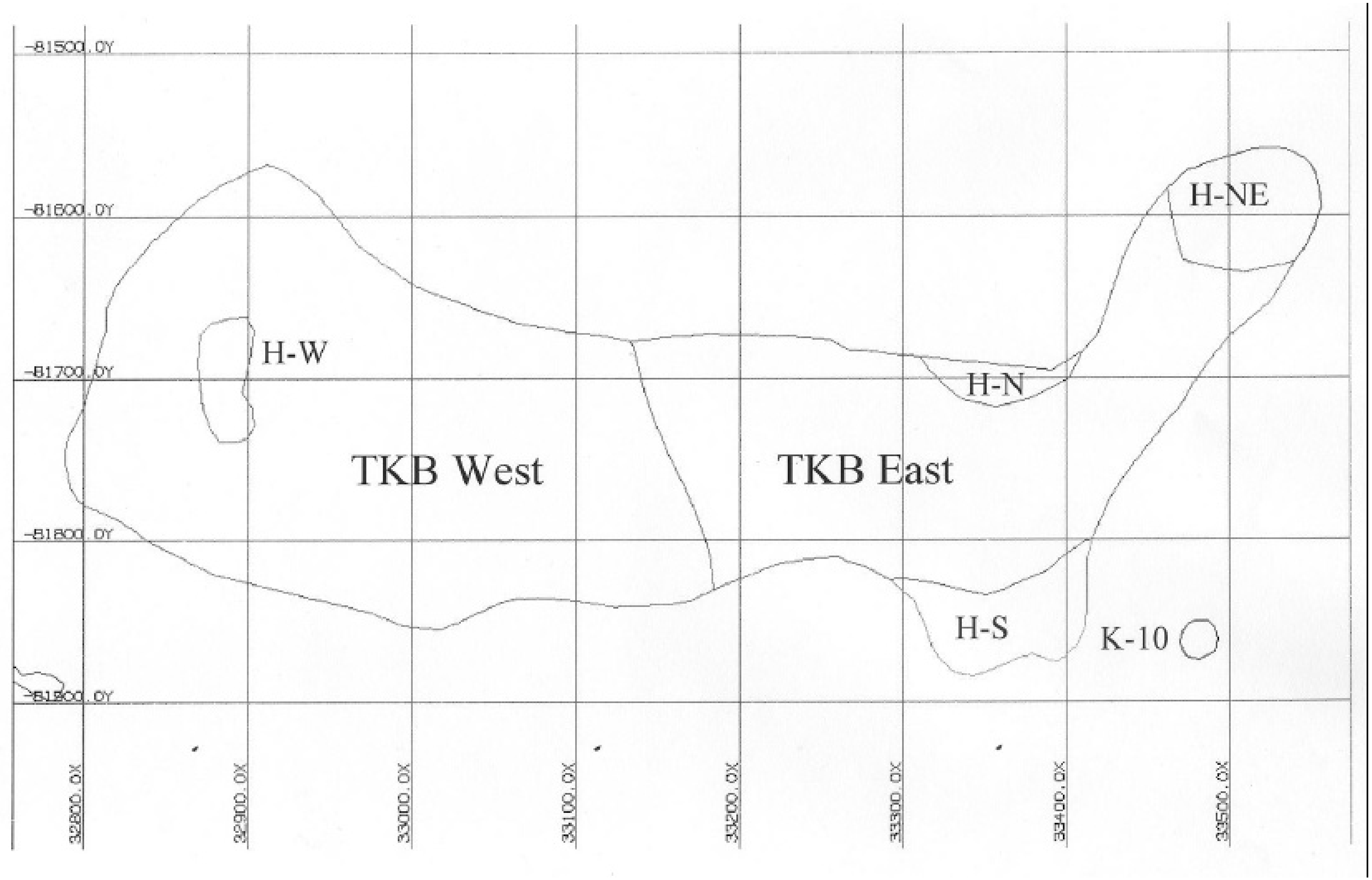

Figure 3: Map showing the kimberlite types presently exposed within the K1 pipe. The bodies are oriented using the local north-south grid and each square is 100 m2. TKB = tuffacitic kimberlite breccia. H = hypabyssal kimberlite. The majority of the nodules in the RAU collection were collected from H-N (hypabyssal north) and H-S (hypabyssal south) on levels 7 through 8 with some from levels 9 and 10.

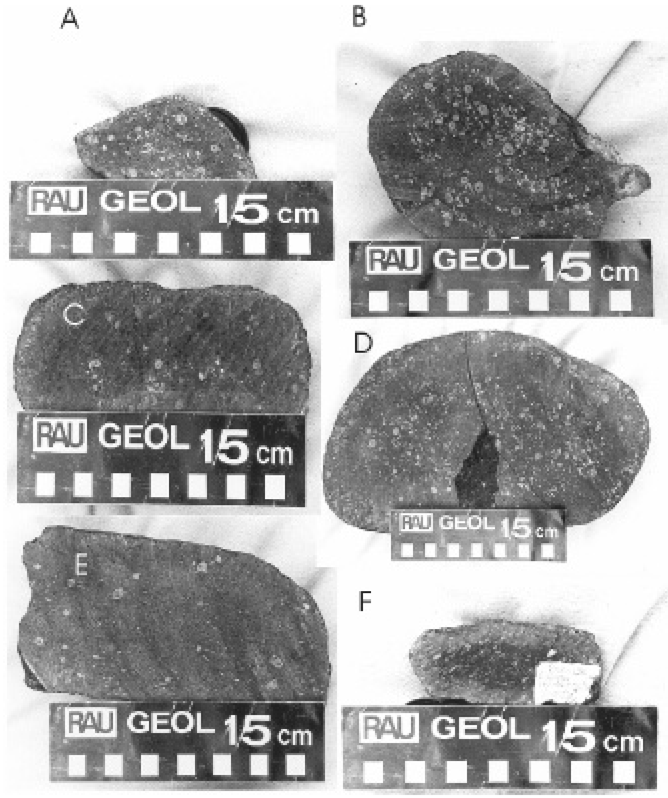

Figure 4: Nodules studied for this manuscript. (A, B and C) VN17, VN19 and B-00-134 respectively; unsheared. Note kelyphitic rims around garnet grains and randomly oriented crystals of orthopyroxene and olivine. In VN-19, note the dark rim around nodule where orthopyroxene and olivine have been serpentinized by reaction with kimberlite magma. In (A), the lack of this rim shows that it is a fragment of a larger nodule. (D and E) B-00-184 and B-00-133 respectively; moderately deformed. Note the winged garnet in the upper left hand corner of E and the kelyphitic rim around it denoting that the rim formed after deformation. Note also the preferred orientation of the orthopyroxene crystals. (F) B-00-136 strongly deformed. Note the linear fabric defined by crystals of orthopyroxene and garnet and the rim around the nodule resulting from reaction with the kimberlitic magma. Olivine grain size has been strongly reduced so that individual grains are not obvious. Note also the smaller size of the strongly sheared nodule compared to the others studied except fragment A, presumably reflecting its inferior resistance to abrasion during transport.

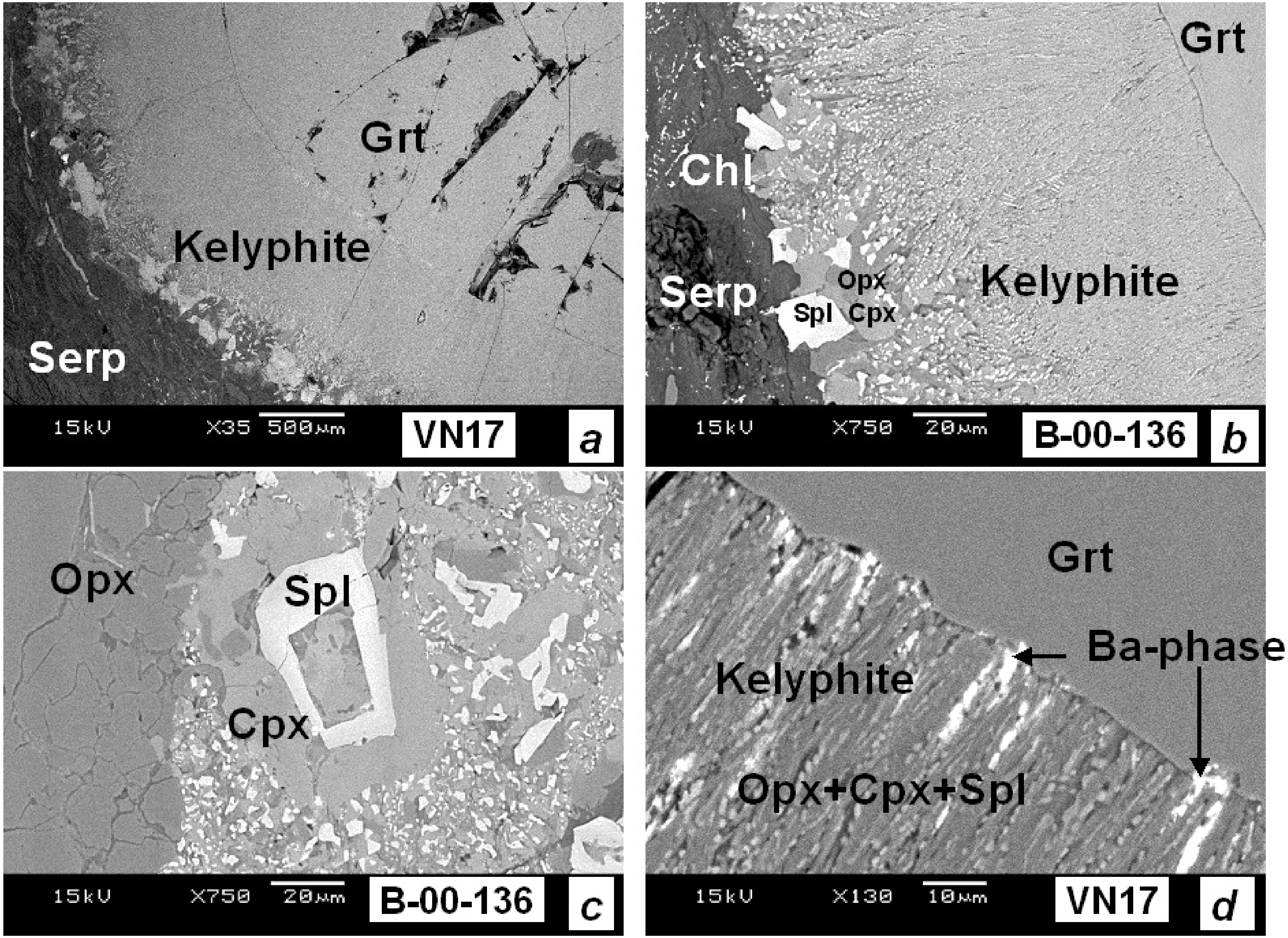

Figure 5: Back-scattered electron images of kelyphitic textures in the samples studied.

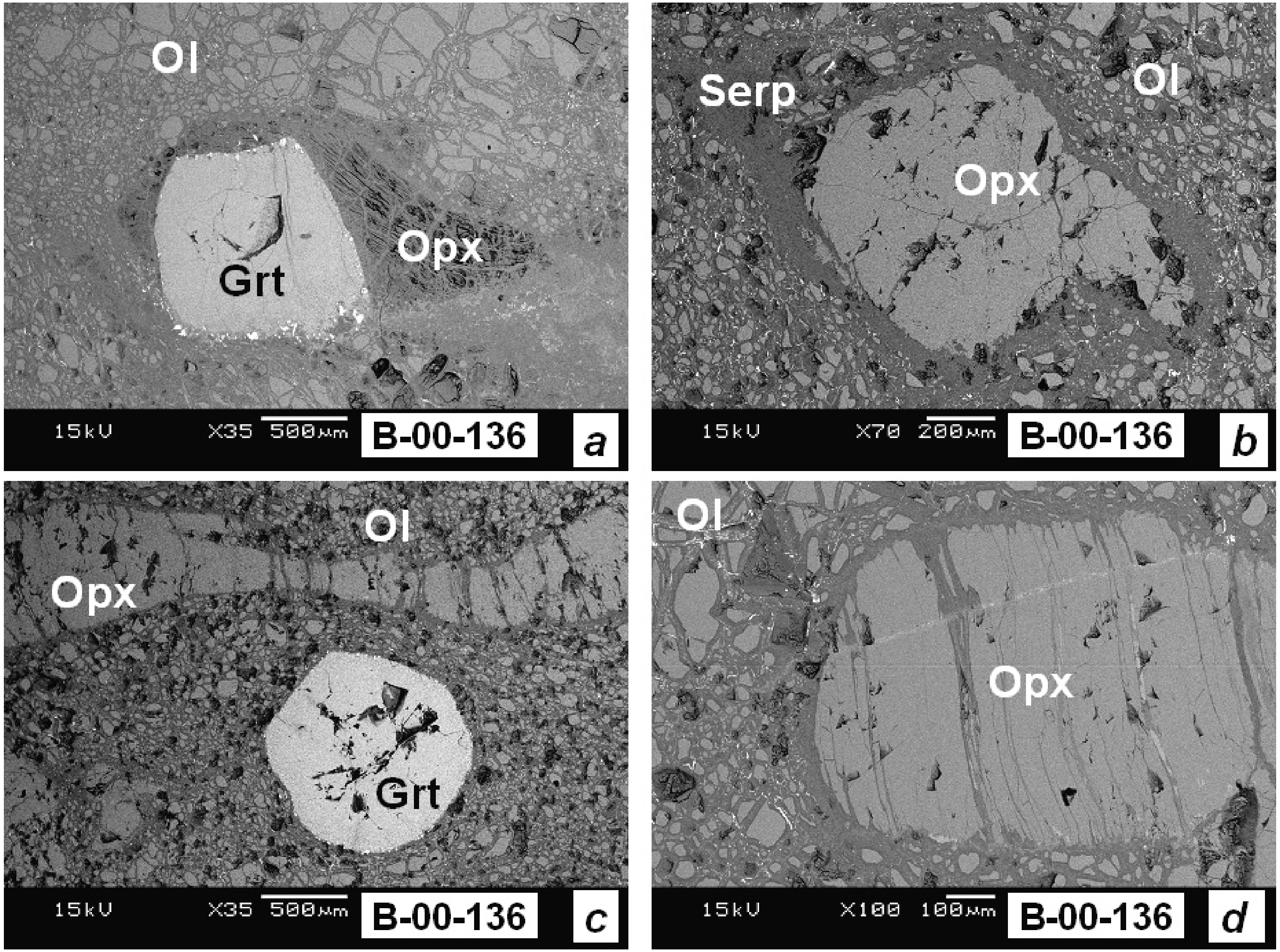

Figure 6: Back-scattered electron images of deformation textures in sample B-00-136.

(*a*) Sigmoid shaped porphyroblast of garnet. (*b*) Delta/sigmoid shaped porphyroclast of orthopyroxene in fine-grained matrix of mylonite composed of olivine and serpentine. (*c*) Ribbon orthopyroxene and garnet porphyroblast in fine-grained matrix of mylonite composed of olivine and serpentine.(*d*) Deformed porphyroblast of orthopyroxene surrounded by olivine and serpentine.

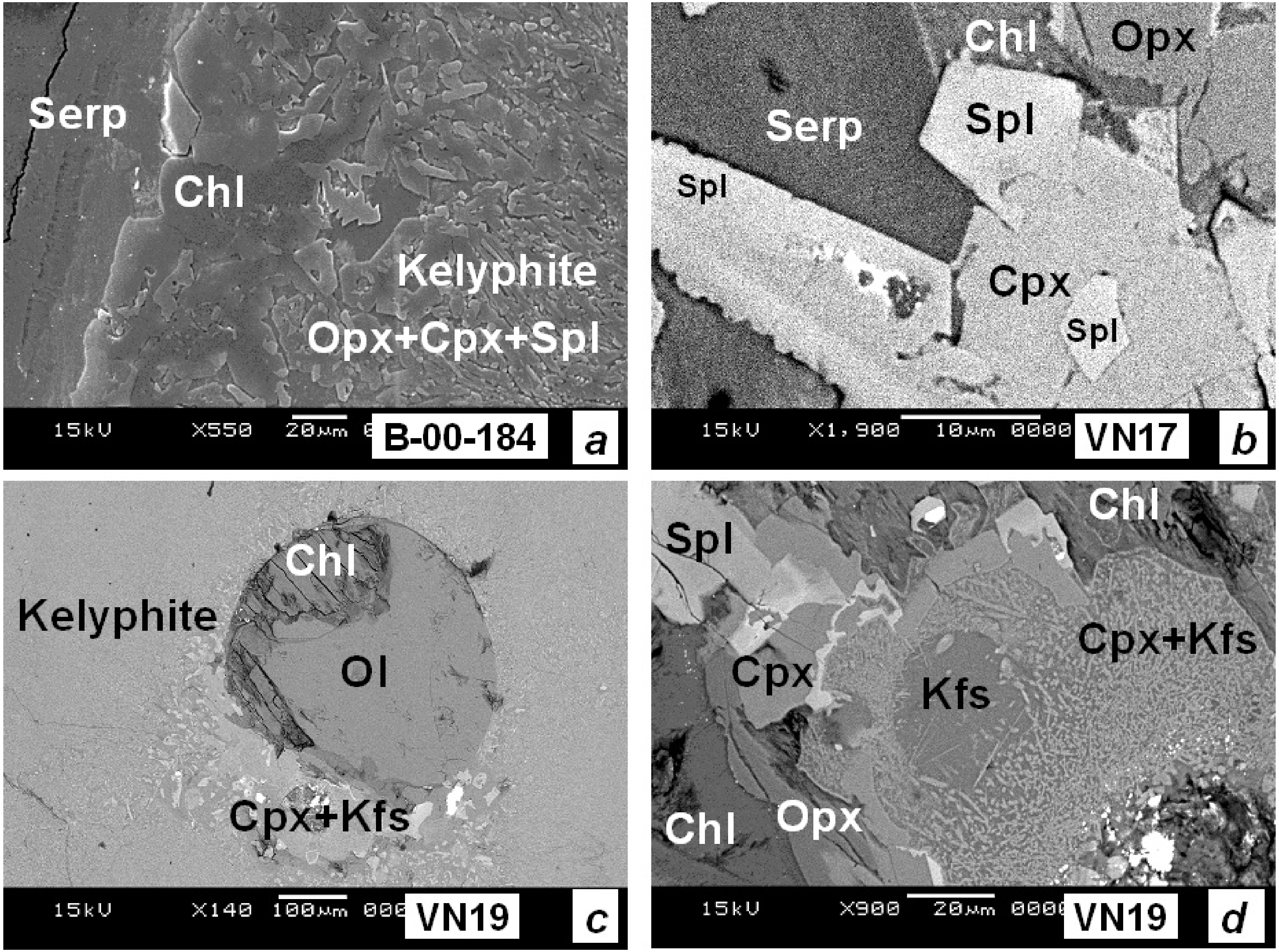

Figure 7: Examples of hydration textures developed in the samples studied.

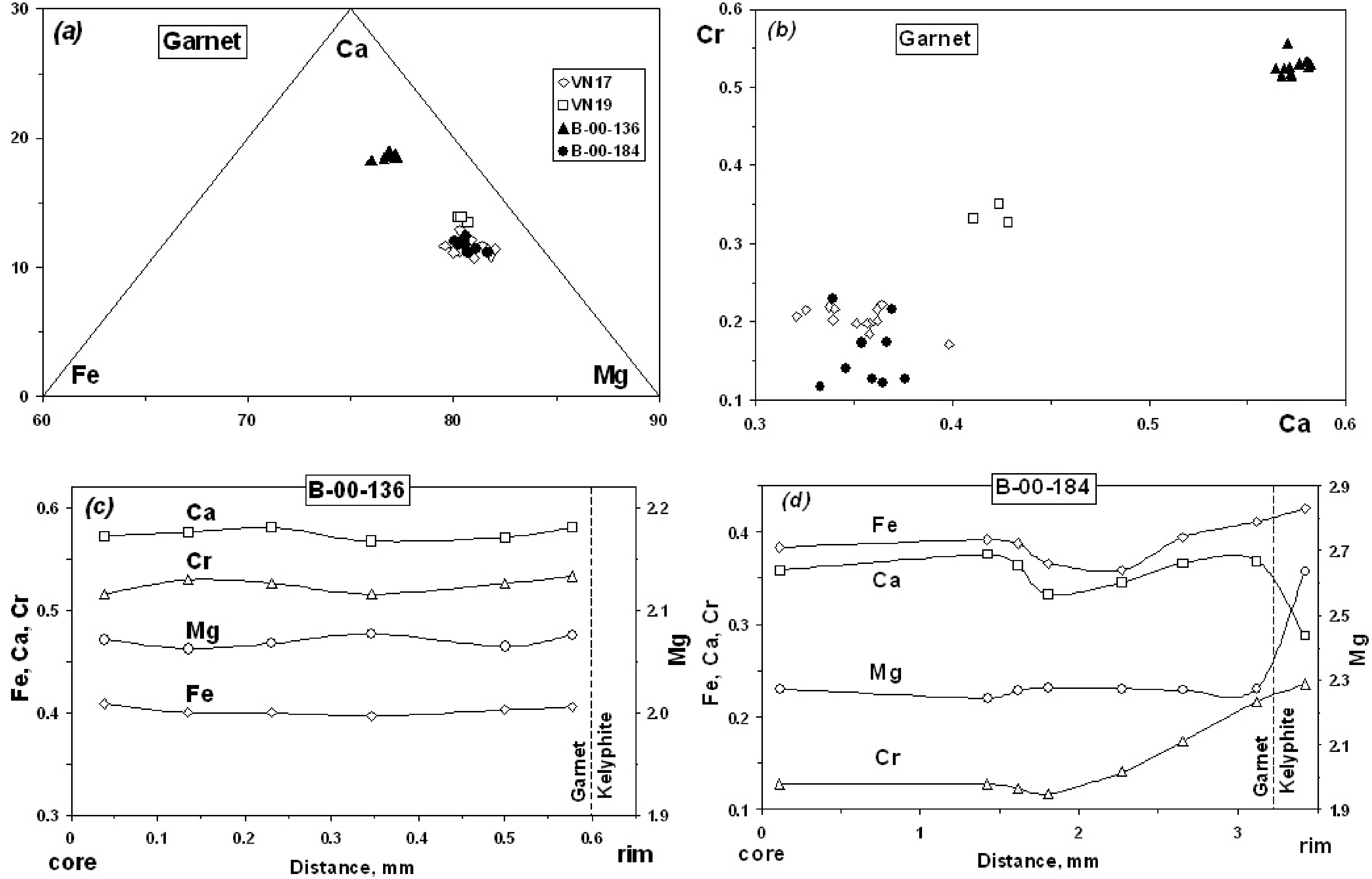

Figure 8: Chemical composition (a) and (b) and zoning (c) and (d) of garnets in the samples studied.

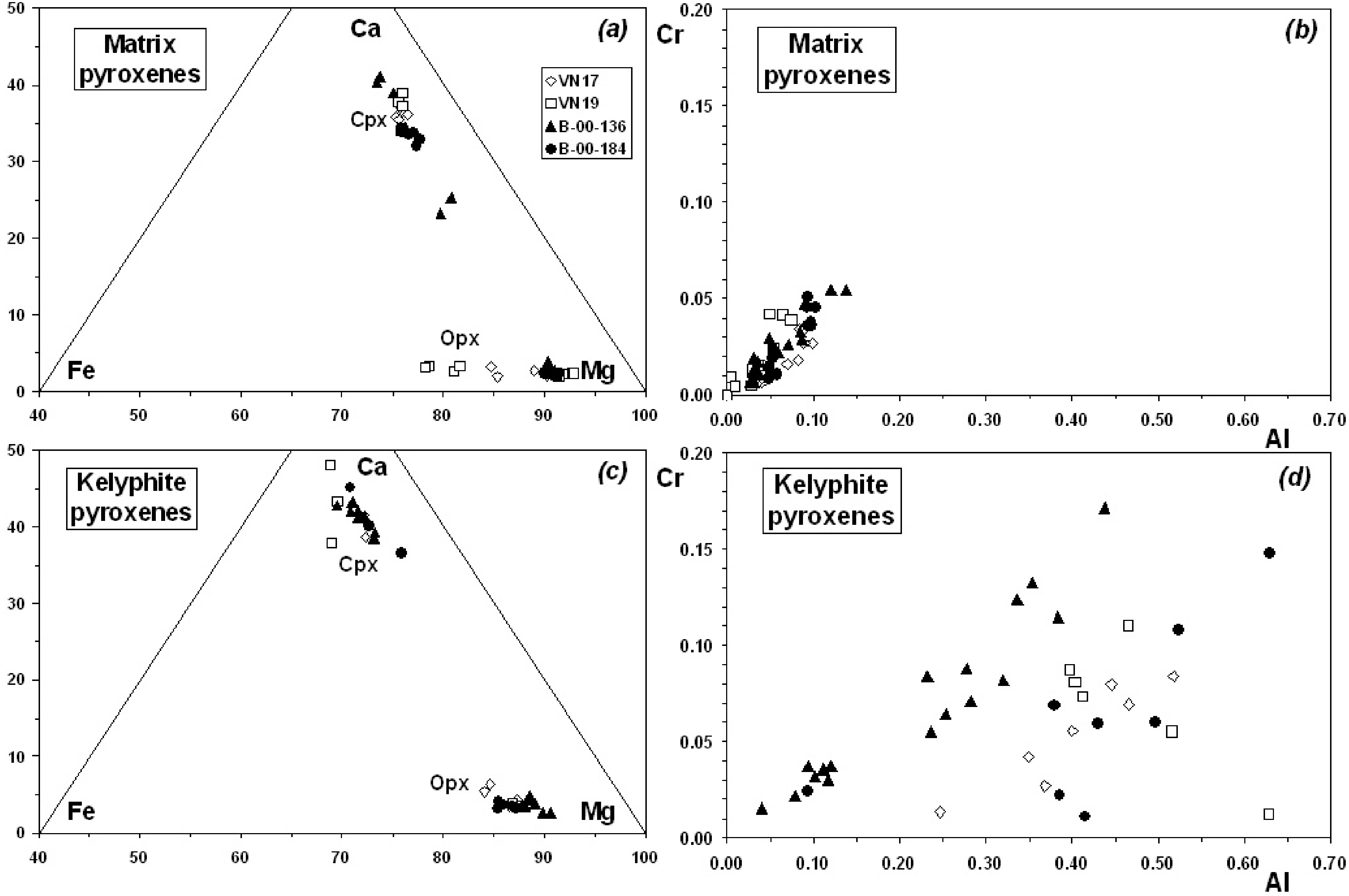

Figure 9: Chemical compositions of matrix (a) and (b) and kelyphite (c) and (d) pyroxenes in the samples studied.

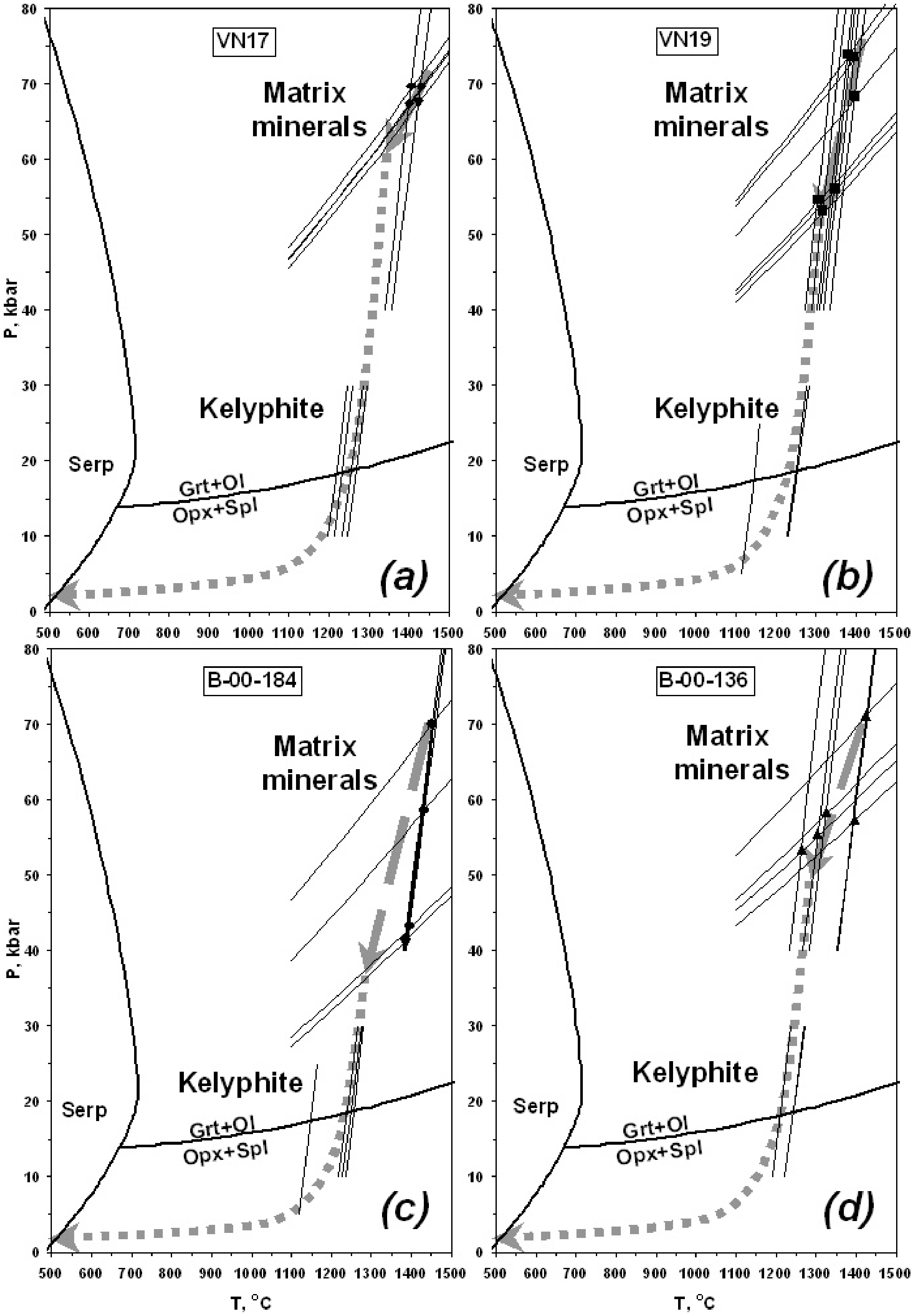

Figure 10: Results of geothermobarometry of samples studied. Thin lines are calculated at the basis of compositions of coexisting minerals using two-pyroxene thermometer (steep lines) and garnet-orthopyroxene barometer (gently sloping lines) of Brey and Kohler (1990). Symbols show individual P-T estimates. Arrows show possible crystallization/deformation (dashed arrows) and exhumation (dotted arrows) trajectories for individual samples. Garnet and serpentine stability fields are after Schmidt and Poli (1999).

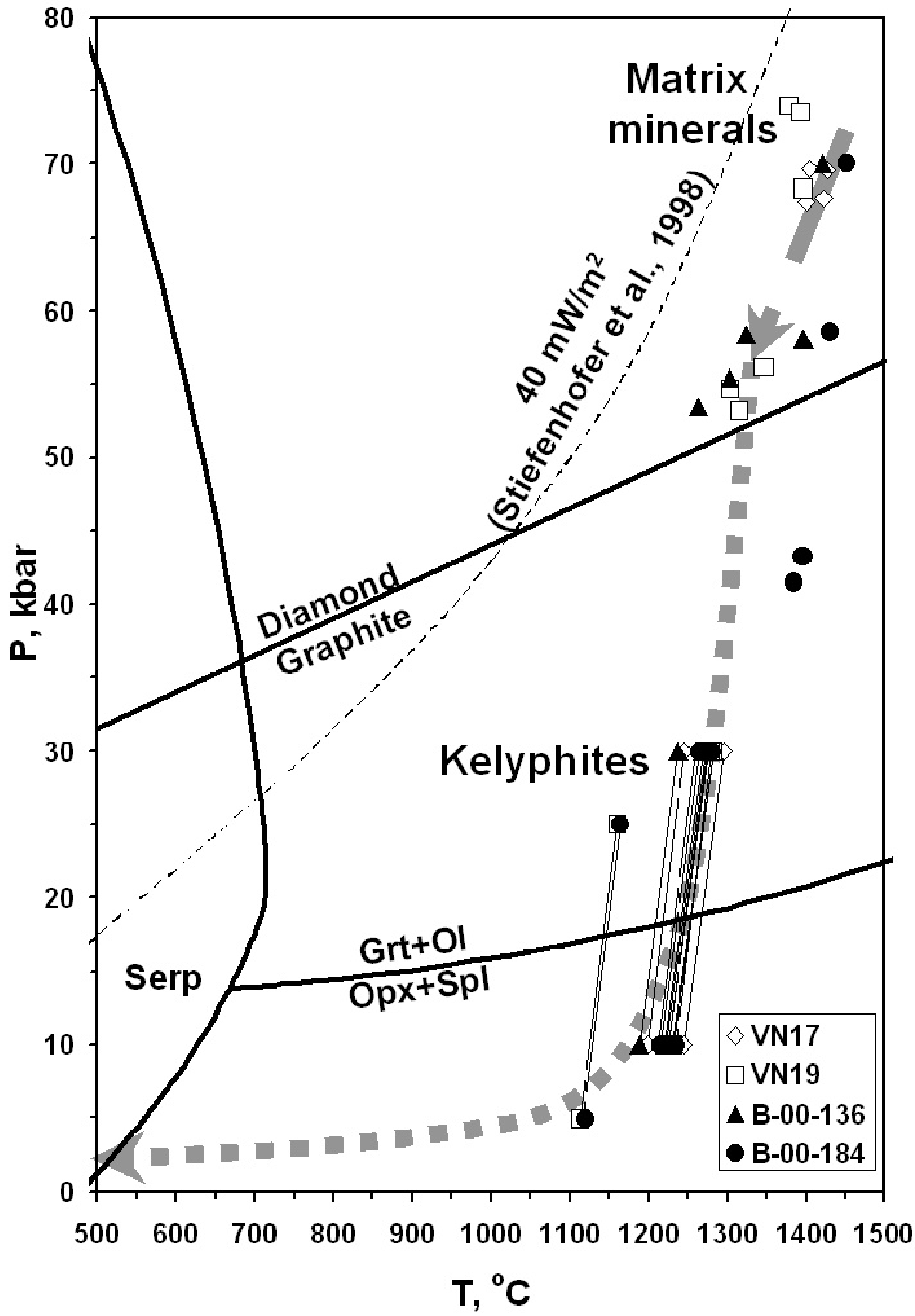

Figure 11: Generalized scheme of the P-T history inferred for studied peridotites. Symbols show individual P-T estimates for different samples calculated using two-pyroxene thermometer and garnet-orthopyroxene barometer of Brey and Kohler (1990). Arrows show possible crystallization/deformation (dashed arrow) and exhumation (dotted arrow) generalized trajectories. Garnet and serpentine stability fields are after Schmidt and Poli (1999). Geotherm suggested by Stiefenhofer *et al.* (1999) is shown for comparison.